MODELING TERAHERTZ DIFFUSE SCATTERING FROM GRANULAR MEDIA USING RADIATIVE TRANSFER THEORY

K. M. Nam[*], L. M. Zurk, and S. Schecklman

Department of Electrical and Computer Engineering, Portland State University, Portland, Oregon 97201, USA

Abstract—Terahertz (THz) spectroscopy can potentially be used to probe and characterize inhomogeneous materials. However, identification of spectral features from diffuse scattering by inhomogeneous materials has not received much attention until now. In this paper, THz diffuse scattering from granular media is modeled by applying radiative transfer (RT) theory for the first time in THz sensing. The diffuse scattered field from compressed polyethylene (PE) pellets containing steel spheres was measured in both transmission and reflection modes using a THz time domain spectroscopy (THz-TDS) system. The RT model was validated by successfully reproducing qualitative features observed in experimental results. Diffuse intensity from granular media containing lactose was then simulated using RT theory. In the results, spectral features of lactose were observed in the diffuse intensity spectra from the granular media.

1. INTRODUCTION

The terahertz (THz) frequency region of the electromagnetic spectrum has recently become available for scientific study and holds great promise for spectroscopic identification of materials [1–4]. However, many materials have granular or volume inclusions, and scattering from these features can obscure or complicate spectral signatures. Since THz sensing will potentially be applied to samples not prepared for laboratory analysis, the question of how to extract spectral signatures from the THz field scattered from inhomogeneities and rough surface interfaces has been a topic of recent attention [5, 6]. The goal of this

work is to study THz scattering from layered granular media using radiative transfer (RT) theory.

Some research has been done in the areas of rough surface scattering effects on reflection measurements [7–10] and volume scattering effects on transmission measurement [6, 11–13]. Diffuse scattering from lactose samples has been measured [7, 8] and a finite-difference time-domain (FDTD) model has been compared with measured diffuse scattering from gold-coated sandpaper [9]. In addition to rough surface scattering, volume scattering from granular inhomogeneities has been studied. THz scattering from granular materials was studied using the quasi-crystalline approximation (QCA) [6, 14, 15]. In addition, the extinction coefficient of different sized grains measured in transmission mode has been compared to Mie theory predictions [11, 12]. Measurements of the transmission of THz waves through random media (arrays of cylinders, textiles, powders, and glass balls) have been used to validate a phase distribution model [16]. Furthermore, THz propagation in strongly scattering random dielectric media has been investigated, using a Monte Carlo model [13]. All these works explored attenuation of coherent energy due to scattering effects in granular random media from transmission measurements.

Scattering in random media has been investigated extensively in microwave and optical ranges. Volume scattering of THz waves, however, has not received the same attention due to the higher absorption of THz waves, the frequency dependent spectral characteristics, and the longer wavelengths [17]. Therefore, appropriate models for scattering in random media are needed to develop spectroscopic identification and/or classification algorithms for THz detection systems.

Analytical wave theory and radiative transfer theory are two methods used to solve scattering problems in random media. The application of analytical theory to real-world problems may be complicated because it is based on a rigorous solution to electromagnetic wave theory, including multiple scattering, interference effects, and diffraction. On the other hand, RT theory is simple and practical as it derived from the transport of energy (or intensity) and it assumes independent scattering [18]. Although the scattering and absorption characteristics of particles come from the principles of wave theory, RT theory itself is relatively simple to solve.

Radiative transfer theory was originally used to study stellar radiation in astrophysics [19], but its use has since spread to other fields. The main applications are active and passive microwave remote sensing and optics, particularly for plane parallel geometries [20, 21].

The RT model has been extended to include a combination of both volume scattering and rough surface scattering [22, 23]. The dense media radiative transfer (DMRT) theory has been applied to the microwave remote sensing of snow [24, 25]. In contrast to the classical radiative transfer theory, DMRT does not start with the transport of energy but is derived from electromagnetic wave theory based on the quasicrystalline approximation, with coherent potential (QCA-CP) for small particles and quasicrystalline approximation (QCA) for moderate size particles [24, 26]. However, DMRT retains the form of the classical radiative transfer equation, so the numerical solution for diffuse intensity can be calculated by the same method [27].

The focus of this paper is to apply the numerical solution of vector radiative transfer equation (VRTE) for plane-parallel medium to THz diffuse scattering from granular inhomogeneities and validate the RT model with measurements using a THz time domain spectroscopy (THz-TDS) system. VRTE includes polarization effects and the numerical solution includes multiple scattering [20]. Both classical RT theory for independent scattering and DMRT theory for dense media are used to model these diffuse scattering effects. This work constitutes the first time RT theory has been applied to THz spectroscopic sensing of solid materials. The next section presents a brief introduction to RT theory. Section 3 describes laboratory measurements of THz-TDS scattering from steel spheres embedded in polyethylene, and compares the results with simulations based on VRTE. RT simulation results for THz scattering from media containing lactose particles are presented in Section 4.

2. RADIATIVE TRANSFER THEORY

This section provides a brief introduction to the concepts and terminology used in VRTE and DMRT theory. More details are available in [25, 28].

2.1. Classical Radiative Transfer Theory

The VRTE for a plane-parallel medium can be used to model the scattered intensity for granular media illuminated by a terahertz source. An important quantity in RT theory is the specific intensity, which is defined as the average power flux density within a unit frequency within a unit solid angle, with units of $[\mathrm{Wm}^{-2}\,sr^{-1}\,\mathrm{Hz}^{-1}]$ (sr = steradian) [18]. In RT theory, the specific intensity quantifies the loss or gain in the incident wave in terms of the extinction coefficient (represents loss of the specific intensity) and the phase
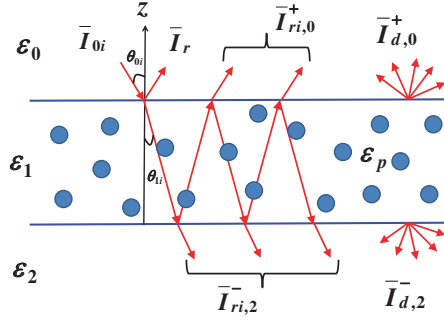
Figure 1. Diagram of the reflected intensity, $\bar{I}_r$, reduced intensity, $\bar{I}_{ri}$, and diffuse intensity, $\bar{I}_d$ observed from a slab containing scatterers illuminated by an obliquely incident intensity, $\bar{I}_{0i}$.

matrix (represents gain in the specific intensity, the redistribution of energy from one propagation direction into another).

Consider an incident electromagnetic plane wave impinging obliquely on a plane-parallel slab containing particles as shown in Figure 1.

The differential change in electric field intensity with distance along the direction of propagation is expressed in the form of the VRTE as follows [20, 26]:

$$\cos\theta \frac{\mathrm{d}}{\mathrm{d}z}\bar{I}(\theta,\phi,z) = -\kappa_e \bar{I}(\theta,\phi,z) + \int\limits_0^{2\pi} \mathrm{d}\phi' \int\limits_0^{\pi} \mathrm{d}\theta' \sin\theta' \overline{\overline{P}}(\theta,\phi;\theta',\phi')\bar{I}(\theta',\phi',z),$$

(1)

where $\bar{I}(\theta,\phi,z)$ is the specific intensity, defined as a vector of four components representing the four Stokes parameters, I_v, I_h, U, and V [29]. The specific intensity, $\bar{I}(\theta,\phi,z)$ is a function of zenith angle θ, azimuth angle ϕ, and depth z. In (1), κ_e is called the extinction coefficient, which is the summation of the scattering coefficient and absorption coefficient, and $\overline{\overline{P}}(\theta,\phi;\theta',\phi')$ is a 4×4 phase matrix, which represents the link between the scattered intensity into the direction (θ,ϕ) from the incident intensity in the direction (θ',ϕ').

The specific intensity can be separated into the reduced intensity and the diffuse intensity [18]. As shown in Figure 1, some amount of incident intensity ($\bar{I}_{0i}$) is reflected at the upper boundary, producing the reflected intensity ($\bar{I}_r$). The rest enters the second medium, which contains particles, and is attenuated as it passes through the medium, resulting in reduced intensity ($\bar{I}_{ri}$). The upward going

reduced intensity is given by $\bar{I}_{ri}^{+}$, while the downward going reduced intensity is given by $\bar{I}_{ri}^{-}$. The reduced intensity represents the coherent intensity traveling in constant direction and its closed form solution is [20, 26]

$$
\begin{aligned}
\bar{I}_{ri}^{+}(\theta,\phi,z) &= \exp\left[-\kappa_e(z+2d)\sec\theta\right]\overline{\overline{F}}(\theta)\overline{\overline{R}}_{12}(\theta)\overline{\overline{T}}_{01}(\theta_{0i})\bar{I}_{0i}, \\
\bar{I}_{ri}^{-}(\pi-\theta,\phi,z) &= \exp(\kappa_e z \sec\theta)\,\overline{\overline{F}}(\theta)\overline{\overline{T}}_{01}(\theta_{0i})\bar{I}_{0i},
\end{aligned}
\tag{2}
$$

where θ_{0i} is the incident angle (as shown in Figure 1), d is a slab thickness, $\bar{I}_{0i}$ is the incident specific intensity, and $\overline{\overline{F}} = \left[\overline{\overline{U}} - \overline{\overline{R}}_{10}(\theta)\overline{\overline{R}}_{12}(\theta)\exp(-2\kappa_e d \sec\theta)\right]^{-1}$ is a matrix that represents infinite reflections from the upper and the lower boundaries [20, 26]. The matrix, $\overline{\overline{U}}$ is an identity matrix. The reflectivity matrix $\overline{\overline{R}}_{ab}$ and the transmissivity matrix $\overline{\overline{T}}_{ab}$ express the relations between the incident and reflected Stokes vectors and between the incident and transmitted Stokes vectors, respectively, at a planar interface between medium a and medium b $(a, b = 0, 1, 2)$ with the permittivity of ϵ_a and ϵ_b, respectively [29].

The diffuse intensity quantifies the incoherent intensity produced from volume scattering and traveling in all directions and the radiative transfer equation for diffuse intensity is given by [26]

$$
\begin{aligned}
\cos\theta\frac{\mathrm{d}}{\mathrm{d}z}\bar{I}_d(\theta,\phi,z) =\ & -\kappa_e\bar{I}_d(\theta,\phi,z) + \int_0^{2\pi}\mathrm{d}\phi'\int_0^{\pi}\mathrm{d}\theta'\sin\theta'\overline{\overline{P}}(\theta,\phi;\theta',\phi')\bar{I}_d(\theta',\phi',z) \\
& + \overline{\overline{P}}(\theta,\phi;\theta_{1i},\phi_{1i})\bar{J}_1(\theta_{1i},\phi_{1i})\exp[-\kappa_e(z+2d)\sec\theta_{1i}] \\
& + \overline{\overline{P}}(\theta,\phi;\pi-\theta_{1i},\phi_{1i})\bar{J}_2(\theta_{1i},\phi_{1i})\exp(\kappa_e z \sec\theta_{1i}),
\end{aligned}
\tag{3}
$$

where θ_{1i} is the transmitted angle associated with the incident angle θ_{0i} from medium 0 to medium 1 (obtained using the Snell's law). The third and the fourth terms of the right-hand side in Equation (3) represent the source of diffuse intensity from the incident intensity of a single scattering event, and $\bar{J}_1$ and $\bar{J}_2$ are given by [26]

$$
\begin{aligned}
\bar{J}_1(\theta_{1i},\phi_{1i}) &= \frac{\epsilon_0 \cos\theta_{0i}}{\epsilon_1 \cos\theta_{1i}}\,\overline{\overline{F}}(\theta_{1i})\overline{\overline{R}}_{12}(\theta_{1i})\overline{\overline{T}}_{01}(\theta_{0i})\bar{I}_{1i}(\pi-\theta_1,\phi_1) \\
\bar{J}_2(\theta_{1i},\phi_{1i}) &= \frac{\epsilon_0 \cos\theta_{0i}}{\epsilon_1 \cos\theta_{1i}}\,\overline{\overline{F}}(\theta_{1i})\overline{\overline{T}}_{01}(\theta_{0i})\bar{I}_{1i}(\pi-\theta_1,\phi_1),
\end{aligned}
\tag{4}
$$

where ϵ_0 and ϵ_1 are the permittivity of medium 0 (the first medium) and medium 1 (the second medium) as shown in Figure 1. In (4),

$\bar{I}_{1i}(\pi - \theta_1, \phi_1) = \bar{F}_o \delta(\cos\theta_1 - \cos\theta_{1i})\delta(\phi_1 - \phi_{1i})$, where $\bar{F}_o$ is the amplitude vector of the incident power flux in the direction (θ_{0i}, ϕ_{0i}) and δ denotes the Dirac delta function, and θ_1 is the transmitted angle of θ_0 (the subscripts, 0 or 1, indicate medium 0 or medium 1, respectively.) and $\phi_1 = \phi_0$.

Numerical methods are utilized to obtain the complete solution of the diffuse intensity. Equation (3) is solved with boundary conditions for diffuse intensity [26],

$$
\begin{aligned}
\bar{I}_d^-(\pi - \theta, \phi, z = 0) &= \overline{\overline{R}}_{10}(\theta)\bar{I}_d^+(\theta, \phi, z = 0) \\
\bar{I}_d^+(\theta, \phi, z = -d) &= \overline{\overline{R}}_{12}(\theta)\bar{I}_d^-(\pi - \theta, \phi, z = -d).
\end{aligned}
\tag{5}
$$

Vector radiative transfer equation for diffuse intensity can be solved numerically [20, 26]. First, the Fourier series is applied to remove ϕ dependence in Equation (3). Next, the integrals in the equations are replaced by a Gaussian quadrature, the solution in terms of N discrete angles (θ). The number N is the half number of angular positions in the range $0° \le \theta \le 180°$. The obtained first order differential equations are solved using the eigenanalysis method and matching boundary conditions. The numerical solution for diffuse intensity can be found in [28].

2.2. Dense Media Radiative Transfer Theory Based on QCA

Radiative transfer theory is applicable to practical problems involving multiple scattering because of its mathematical simplicity. However, using an independent scattering assumption limits its use to a low fractional volume of particles. As the fractional volume of particles increases, the scattering will be influenced by the coherent wave interaction among the particles. In this paper, dense media radiative transfer (DMRT) theory based on the quasi-crystalline approximation (QCA) [25] is used to model high fractional volume granular media.

In the DMRT theory, the extinction coefficient and phase matrix are obtained using QCA. QCA is an analytical method to solve multiple scattering problems based on scattering equations derived from Maxwell's equations. The coherent and incoherent fields are calculated statistically from the multiple scattering equations, and a hierarchy of the equations is generated. Truncation is made at the second stage of the hierarchy of equations in QCA. In contrast to independent scattering, the positions of particles in a dense medium affect the scattering of electromagnetic waves. Therefore, a pair distribution function describes the particle positions. The details of calculating the extinction coefficient and phase matrix can be found

in [25, 28]. The reduced intensity and the diffuse intensity can be obtained through the same procedure as in classical RT theory.

3. TERAHERTZ SCATTERING MEASUREMENTS

This section describes laboratory measurements of THz-TDS scattering from volume scatterers (spherical steel scatterers) embedded in polyethylene (PE), and compares the results with simulations based on the classical RT theory. The measurements of THz diffuse scattered field were performed by using a THz-TDS system (Picometrix T-ray 4000). Measurements were conducted using a variety of measurement geometries in both transmission and reflection mode, for samples with differing layer thickness and particle concentration.

3.1. Experimental Setup and Data Processing

3.1.1. Sample Preparation and Experimental Setup

Two different samples were prepared to measure the diffuse scattering caused by granular media. For both samples, the background material was PE with grains less than $10\,\mu m$ in diameter, and the steel spheres (which were used for volume scatterers because they produce sufficiently strong scattering to enable an accurate measurement of diffuse field) had a 1 mm diameter. The spheres were made of AISI Type 52100 steel, which is composed primarily of iron [30]. The spheres were evenly distributed in the PE powder, and the mixed powder was pressed in a hydraulic press (at 1 ton for 1 minute) resulting in pellet samples with a diameter of 4 cm. The sample thickness and fractional volume of the metal spheres are 5 mm and 2% for sample 1 and 9.5 mm and 3.2% for sample 2, respectively, as shown in Table 1.

Terahertz scattering measurements were performed using a Picometrix T-Ray 4000 THz-TDS system in the Northwest Electromagnetics and Acoustics Research Laboratory (NEAR-Lab) at Portland

Table 1. Fractional volume of metal spheres, f_v, and the thickness, d, of two pellet samples (compressed PE powder containing steel spheres).

	Fractional volume (%)	Thickness (mm)
Sample 1	2	5
Sample 2	3.2	9.5

(a) Transmission Mode   (b) Reflection Mode

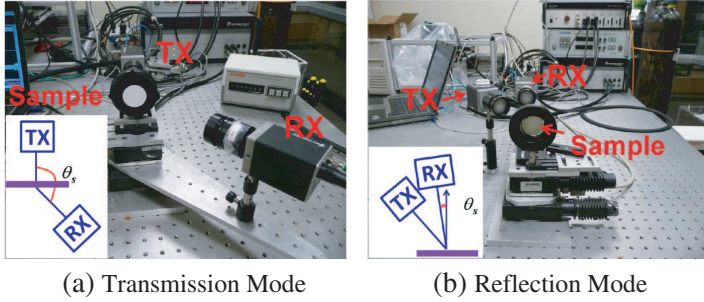**Figure 2.** Experimental setup for (a) transmission measurement at a normal incidence, $\theta_i = 0°$ and $\theta_s = 140°$ and (b) reflection measurement at an oblique incidence, $\theta_i = 29°$ and $\theta_s = -6°$.

State University. The T-Ray 4000 is composed of a main module (containing a femto-second laser, beam splitter and mirrors) and fiber-optic cables connected to two remote heads that transmit (TX) and receive (RX) THz waves. For these experiments the TX head was fixed in place and the RX head was moved to various observation angles on a computer-controlled arm centered beneath the sample, as shown in Figure 2. The sample was mounted on a holder which could be rotated between measurements to provide independent scattering realizations from the spheres randomly embedded in the PE. Both the TX and RX heads used collimating lenses oriented for vertical polarization.

Transmission measurements at normal incidence ($\theta_i = 0°$) were conducted at a number of observation angles ($\theta_s = 180°, 160°, 140°,$ and $120°$) as shown in Figure 2(a). Reflection measurements with an angle of incidence of $\theta_i = 29°$ were taken at the specular angle ($\theta_s = 29°$) and at a diffuse angle ($\theta_s = -6°$). The negative sign of the scattering angle ($-6°$) is conventional notation to indicate the left side of the normal as shown in Figure 2(b).

3.1.2. Signal Processing

The scattered field from sample pellets was measured in THz time domain. Coherent averaging of multiple waveforms lowers the noise floor, increasing SNR. In these measurements, 10,000 time-domain waveforms were averaged for each diffuse scattering measurement. The THz waveforms (field) in time domain were transformed to the power spectral densities by performing a fast Fourier transform (FFT). Deconvolution processing was then performed by normalizing the sample measurement with the reference measurement in order

to remove the effects of the response of the whole system. For transmission measurements the reference was a transmission measurement with no sample in the holder. The reference for reflection measurements was a specular reflection from a smooth conductor.

The RT theory predicts the intensity of the coherent and incoherent field components. In experimentation, the coherent field can be estimated with a Monte Carlo approach by averaging over multiple realizations [31, 32]. Each realization contains a different ensemble of scatterers, but with the same statistics (i.e., same sphere radius, fractional volume, etc. arranged randomly in the volume). At angles other than the direction of the coherent field (for example, in reflection mode at non-specular angles, $\theta_s \neq \theta_i$), only the incoherent field should be present and the average field should approach zero. However, with a finite number of realizations it may be difficult to get sufficient averaging, and thus the data used here was smoothed to remove residual effects. In this experiment, 36 realizations of measurements for each sample pellet were carried out to obtain statistical average of the realizations. Half of the 36 realizations were from one side of the sample and half were from the other. For the 18 realizations per side, the sample was rotated in 20 degree increments through 360 degrees. The frequency domain spectra for the 36 realizations were averaged.

3.1.3. Simulation Process Using RT Theory

The numerical solutions of the classical RT equation for a plane parallel slab is used to model the compressed PE pellets containing randomly distributed metal spheres. The parameters to calculate the specific intensity for the two samples are the sphere size with radius $a = 500\,\mu m$, the permittivities of the surrounding media $\epsilon_0 = 1$ and $\epsilon_2 = 1$, and the background medium (PE) $\epsilon_1 = 2.1316$. The permittivity of scatterers was assumed to be $\epsilon_p = -5 \times 10^4 + i4 \times 10^5$ which is an approximate value for Iron in THz frequency region from [33]. The sample thickness and fractional volume of the metal spheres are given in Table 1.

Different numbers of discretizing angles (N) in the region of the measured angles are chosen to explore sensitivity to numerical discretization. Therefore, the measured data at 160°, 140°, and 120° are compared with the RT simulation at 159.9° $(N = 18)$, 139.7° $(N = 16)$, and 120.2° $(N = 14)$, respectively, in transmission mode. Also, the measured data at −6° is compared with the RT simulation at −6.2° $(N = 16)$ in reflection mode.

The diffuse specific intensity (I_d) calculated from the numerical simulation was converted into normalized intensity (I) in order to compare theoretical results with measured results using the following

formula [34]:

$$I = \Delta\Omega I_d \approx \pi\theta_d^2 I_d \tag{6}$$

where $\Delta\Omega$ is the detector's field of view (FOV), and the detector's half angle beam width, θ_d, is assumed to be small. The detector's half angle beam width is on the order of

$$\theta_d \propto \frac{\lambda}{2D} \tag{7}$$

where D is the linear dimension of a receiver and λ is a wavelength. Equation (7) comes from the far-field beam width (full-width at half-maximum) for a radiator of linear dimension D using the reciprocity theorem. The detector's field of view can be calculated using Equations (6) and (7)

$$\Delta\Omega \approx \pi\theta_d^2 \approx \pi\left(\frac{\lambda}{2D}\right)^2 \approx \pi\left(\frac{c}{2Df}\right)^2 \tag{8}$$

where c is the speed of light and f is a frequency. The detector's half angle beam width was approximated to be $4°$ at 0.1 THz and the FOV is scaled to $1/f^2$ as frequency increases.

3.2. Comparison of Data and Theory

3.2.1. Transmission Measurements

Figure 3 shows the comparison between the normalized intensity for the measured data and that for the simulation results in transmission mode (corresponding to Figure 2(a)). The transmitted intensity is the sum of the reduced intensity, I_{ri}, and diffuse intensity, I_d. Since the measured field at $\theta_s = 180°$ is dominated by the coherent field, the transmitted intensity is modeled as the reduced intensity alone from Equation (2) because it is much stronger than the diffuse intensity. Transmitted energy at all angles are produced from volume scattering, and thus the transmission measured at $\theta_s = 160°$, $140°$, and $120°$ were modeled as diffuse intensity from Equation (3).

Figure 3(a) shows the transmitted intensity at $\theta_s = 180°$, and the measured intensity was only a few dB (1–2 dB) lower than the simulated values. Sample 2 shows a lower normalized intensity than sample 1 for both the measured and simulated data. This is to be expected because sample 2 is thicker and has a higher fractional volume of scatterers. The optical depth ($\tau = \kappa_e \times d$) is approximately 1.0 for sample 2 and 0.33 for sample 1. Thus, the second part of Equation (2) indicates that sample 2 would have a lower value for the
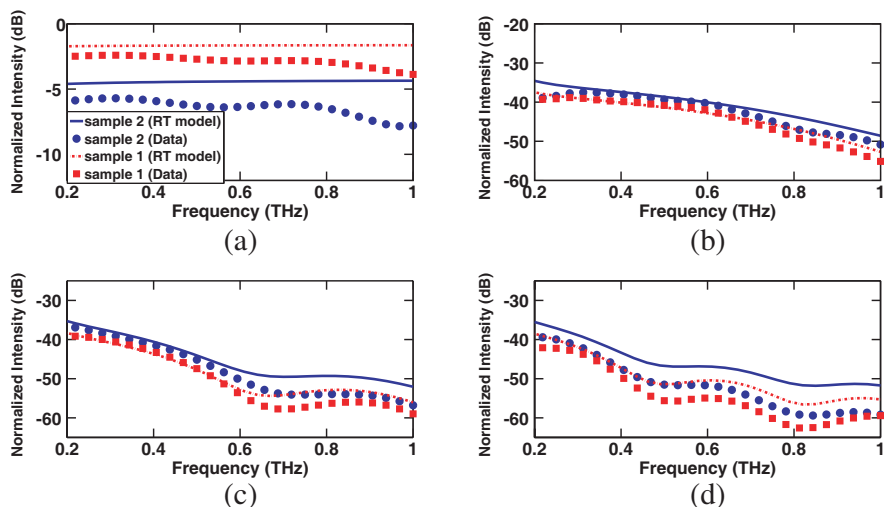
Figure 3. Comparison between the normalized intensity of measured data and simulated results in transmission mode with normal incidence ($\theta_i = 0°$): (a) the reduced intensity at $\theta_s = 180°$, and (b) the diffuse intensity at $\theta_s = 160°$, (c) at $\theta_s = 140°$, and (d) at $\theta_s = 120°$. Steel spheres ($500\,\mu$m in radius) embedded in PE powder were used for pellet samples (sample 1: $f_v = 2\%$, $d = 5$ mm, and sample 2: $f_v = 3.2\%$, $d = 9.5$ mm). Radius of samples is 2 cm.

reduced intensity. Since sample 2 contains a higher fractional volume of scattering particles, it scatters more energy away from the straight-line transmission direction, $\theta = 180°$, and into diffuse directions. This is observed for the measured and simulated data at diffuse observation angles $\theta_s = 160°$, $\theta_s = 140°$, and $\theta_s = 120°$, as shown in Figures 3(b), 3(c), and 3(d), respectively.

In general, the RT simulations for diffuse intensity shown in Figures 3(a)–3(d) demonstrate relatively good agreement with the levels and trends observed in the measurements. However, there was some small disagreement (on the order of a few dB) between the measurements and simulations which increased with scattering angle and frequency. The exact cause(s) for these behaviors is not known at this time, but may be due to the way the experiment was modeled. The model assumes the incident beam is an infinite plane wave and that the background medium is homogeneous and of infinite extent. In the measurements the incident beam is a finite quasi-Gaussian wave with frequency-dependent beam size, incident on a background medium that is composed of tightly packed polyethylene grains. The amount

of pressure and time needed to tightly compress the PE grains is unknown. Therefore, the size and/or fractional volume of the air voids in the samples may have been sufficient to cause significant scattering at higher frequencies. The techniques necessary to tightly pack powder grains remains an open topic for future work. In addition, in the model, the detector is assumed to be a point detector which detects a diffuse specific intensity only in the observed direction. The measured intensity is composed of the sum of all of the diffuse specific intensities that enter the detector's aperture. Equations (6)–(8) were used to approximate the normalized intensity at the measurement detector as discussed in Section 3.1.3.

An interesting observation is that the diffuse intensity at $\theta_s = 140°$ has one distinct spectral feature (a null near 0.7 THz) as shown in Figure 3(c). Also, Figure 3(d) shows two distinct features (nulls near 0.5 THz and 0.8 THz) at $\theta_s = 120°$. The nulls appear in both simulations and measurements. In contrast, there are no nulls in the simulations or measurements at 180° and 160°. The nulls might be due to Mie scattering of the steel spheres. The size parameter of steel spheres in PE powder background ranges from 3.1 to 15.3 for frequencies between 0.2 and 1 THz.

3.2.2. Reflection Measurements

Figure 4 shows the comparison between the normalized intensity for the measured data and that for the simulation results in reflection mode (corresponding to Figure 2(b)). The first measurement was used to explore the amount of coherent energy reflected at the boundary between two media (air and PE pellet containing steel spheres). The second set of measurements was used to explore the amount of diffuse scattering energy in reflection mode.

Figure 4(a) shows the normalized intensity for sample 1 at the specular angle in reflection mode and also its values were adjusted by shifting the levels (re-normalization by dividing each values by the values of the 1st pulse for RT model. The reflected intensity (1st pulse) is the bounced wave at the upper boundary surface and the reduced intensity (2nd pulse) is the wave that bounced from lower boundary surface. The second pulse is weaker than the first pulse because the coherent energy passing through the scattering medium is attenuated.

Figure 4(b) shows the comparison between the measurement and simulation at off-specular angle in reflection mode. The normalized diffuse intensity for sample 2 is stronger than sample 1 in both the experimental and simulated results because sample 2 is thicker and has a higher fractional volume of scatterers than sample 1.
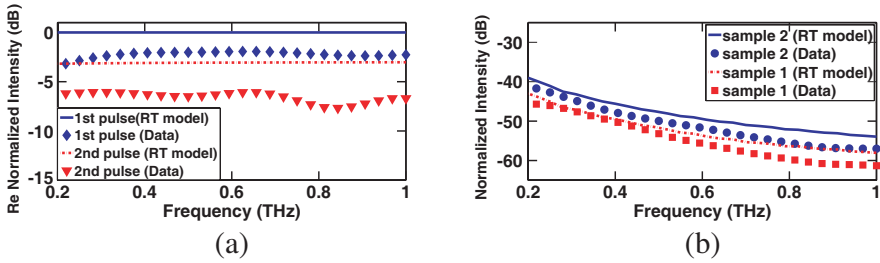
Figure 4. Comparison between the normalized intensity of measured data and simulated results in reflection mode with oblique incidence ($\theta_i = 29°$): (a) (1st pulse) the reflected intensity bounced at the upper boundary of sample 1 and (2nd pulse) the summation of the reduced intensity and diffuse intensity at specular angle. The reduced intensity was bounced at the lower boundary once, but not multiple times. The diffuse intensity is negligible. Each plot was shifted to make the 1st pulse for the RT model to be located at 0 dB. (b) The diffuse intensity at off-specular angle $\theta_s = -6°$.

The RT simulations shown in Figures 4(a) and 4(b) demonstrate relatively good agreement with the levels and trends observed in the measurements. The exact cause(s) for the small disagreement (on the order of a few dB) between the measurements and simulations is not known at this time, but may be due to the way the experiment was modeled as discussed in the previous section.

4. SIMULATION RESULTS

This section presents simulation results for diffuse scattering from granular media using the RT theories. Diffuse scattering is present in all directions in both transmission and reflection geometries, while coherent energy propagates in a single direction (the specular direction). In the previous section, neither material had spectral features (PE and steel were approximately independent of frequency), but in this section, we will explore diffuse scattering from granular media whose material has spectral features. Lactose (which has spectral absorption signatures in the THz frequency range) grains are used for scatterers embedded in an PE background. The diffuse scattering is governed by various factors such as the material properties of the particles, their sizes, and concentration (number of particles per unit volume) in the medium, the material properties of the background media, the thickness of the medium, the surrounding media, and

the incident wavelength. In this work, the relationship between the material properties of the grains and the diffuse intensity is investigated by varying the grain size, concentration, and layer thickness because we are interested in detection of material of media from diffuse intensity.

For these simulations, both incident and scattered waves are assumed to have vertical polarization. The incident angle is $\theta_i = 30°$, and the scattering angles are $\theta_s = 30°$ in reflection mode (backscattering), and $\theta_s = 150°$ in transmission mode, respectively, as shown in Figure 5(a). The calculation was performed using $\theta_i = 31.21°$ and $\theta_s = 31.21°$ in reflection mode and $\theta_s = 148.79°$ in transmission mode determined by choice of Gaussian quadrature. The permittivity for the background medium is $\epsilon_1 = 2.1316$ (PE), and for the surrounding media, $\epsilon_0 = \epsilon_2 = 1$. The diffuse intensity is calculated using the classical RT model for low fractional volume of scatterers (5%) and the DMRT model based on QCA for high fractional volume (20%). In these simulations, an important condition is that the parameter size, ka, is too low to exhibit Mie resonance effects in the frequency spectra.

Figure 5(b) shows the real and imaginary permittivities of lactose and they have spectral signatures in the THz frequency range. The difference between the real part of lactose grain permittivity and PE background permittivity causes scattering and the imaginary permittivity of lactose grain causes absorption.

Figures 6(a) and 6(b) show the predicted diffuse specific intensities for a reflection mode geometry. As the radius of the lactose grains increases from 25 μm to 50 μm (solid line to dotted line), the diffuse specific intensity increases for low frequencies. In contrast, particle size has a decreasing effect on diffuse specific intensity at high frequencies.
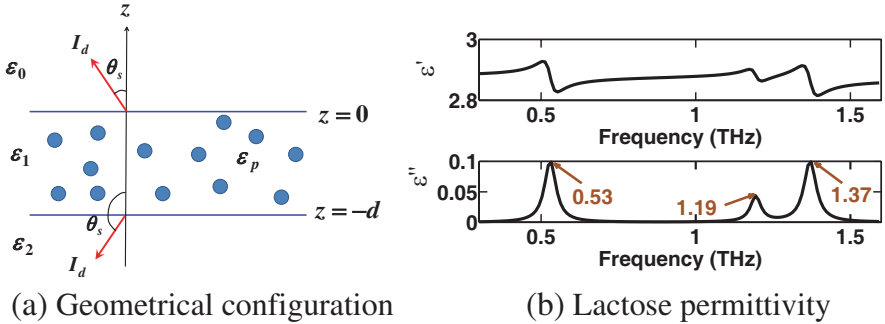

(a) Geometrical configuration   (b) Lactose permittivity

Figure 5. (a) Geometrical configuration assumed in RT simulation, and (b) lactose permittivity: real part ϵ' and imaginary part ϵ''.

(a) Reflection: $f_v = 5\%$, $d = 5$ mm   (b) Reflection: $f_v = 20\%$, $d = 10$ mm

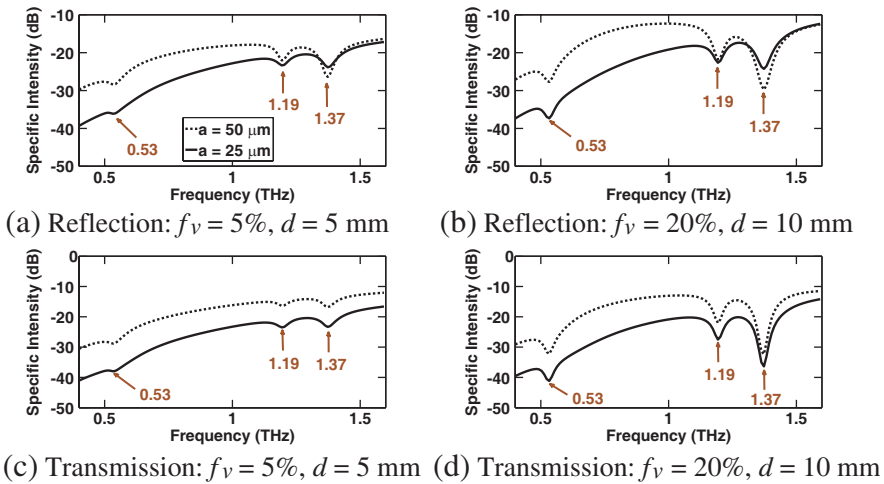(c) Transmission: $f_v = 5\%$, $d = 5$ mm (d) Transmission: $f_v = 20\%$, $d = 10$ mm

Figure 6. The diffuse specific intensities for slabs with randomly distributed lactose grains ($25\,\mu$m or $50\,\mu$m in radius, a) in PE background ($\epsilon_1 = 2.1316$) (a) for fractional volume of lactose grains, $f_v = 5\%$, and slab thickness, $d = 5$ mm, in reflection mode, (b) for $f_v = 20\%$ and $d = 10$ mm in reflection mode, (c) for $f_v = 5\%$ and $d = 5$ mm in transmission mode, and (d) for $f_v = 20\%$ and $d = 10$ mm in transmission mode.

Interestingly, three narrow spectral features are shown at 0.53 THz, 1.19 THz, and 1.37 THz, which are the same frequencies for imaginary permittivity peaks of lactose. The depth of nulls is affected by fractional volume of grains, thickness of layer, and particle size, but the frequencies for spectral features are unaffected and no new frequencies are introduced by the particle scattering. In reflection mode, we can see the spectral features of the imaginary permittivity of lactose in the diffuse intensity.

Figures 6(c) and 6(d) show the diffuse specific intensities in transmission mode. Even though the specific intensity for larger grains is stronger than that for smaller grains, the spectral features do not change. The three spectral features of imaginary permittivity of lactose are also shown in the transmission mode data.

In both reflection and transmission modes, we could identify lactose from diffuse scattering intensity. This simulation result indicates that under certain conditions (e.g., no Mie resonances), a medium containing grains with THz spectral features may be identified from diffuse scattering intensity.

5. CONCLUSIONS

Volume scattering from granular media in THz frequency region was studied using radiative transfer theory. Polarization and multiple scattering effects were included by using the vector radiative transfer equation and solving the equation numerically. Since RT theory (called classical RT theory) is limited to low fractional volume, dense media radiative transfer (DMRT) theory based on QCA for dense media was applied to the case for high fractional volume.

The RT model was validated by laboratory measurements using two compressed PE pellets containing steel spheres. The measurement results showed two extreme cases of energy redistribution. For highly scattering medium, the reduced intensity is strongly attenuated. This energy is redistributed in the form of diffuse intensity, so the diffuse intensity is very strong. For weakly scattering medium, there is very little diffuse intensity and therefore the change in the reduced intensity is also small. In addition, angle dependent spectral features due to Mie scattering were observed.

Diffuse volume scattering from random media containing lactose grains was investigated using the RT models. The simulation results showed that the diffuse intensity was affected by the material properties of grains as well as other factors such as grain size, fractional volume of grains, and thickness of scattering layer. The medium containing grains with THz spectral features showed some spectral features in its diffuse intensity spectra even though grain size, fractional volume of grains, and thickness of scattering layer affect the diffuse intensity spectra. The simulation results indicated that it is possible to identify materials from diffuse intensity spectra.

ACKNOWLEDGMENT

REFERENCES

1. Mickan, S. P. and X.-C. Zhang, "T-ray sensing and imaging," *Int. J. High Speed Electron. Syst.*, Vol. 13, No. 2, 601–676, 2003.
2. Van Exter, M. and D. R. Grischkowsky, "Characterization of an optoelectronic terahertz beam system," *IEEE Trans. Microwave Theory Tech.*, Vol. 38, No. 11, 1684–1691, 1990.
3. Kemp, M. C., P. F. Taday, B. E. Cole, J. A. Cluff, A. J. Fitzgerald, and W. R. Tribe, "Security applications of terahertz technology," *Proc. SPIE Int. Soc. Opt. Eng.*, Vol. 5070, 44–52, 2003.

4. Federici, J. F., B. Schulkin, F. Huang, D. Gary, R. Barat, F. Oliveira, and D. Zimdars, "THz imaging and sensing for security applications — Explosives, weapons and drugs," *Semicond. Sci. Technol.*, Vol. 20, No. 7, S266–S280, 2005.

5. Zeitler, A. (ed.), *Terahertz spectroscopy: Theory and Applications*, Springer Press, 2012.

6. Zurk, L. M., B. Orlowski, D. P. Winebrenner, E. I. Thorsos, M. R. Leahy-Hoppa, and L. M. Hayden, "Terahertz scattering from granular material," *J. Opt. Soc. Am. B*, Vol. 24, No. 9, 2238–2243, 2007.

7. Arbab, M. H., A. Chen, E. I. Thorsos, D. P. Winebrenner, and L. M. Zurk, "Effect of surface scattering on terahertz time domain spectroscopy of chemicals," *Proc. SPIE Int. Soc. Opt. Eng.*, Vol. 6893, 2008.

8. Henry, S. C., G. P. Kniffin, S. Schecklman, L. M. Zurk, and A. Chen, "Measurement and modeling of rough surface effects on terahertz spectroscopy," *Proc. SPIE Int. Soc. Opt. Eng.*, Vol. 7601, 2010.

9. Sundberg, G., L. M. Zurk, S. Schecklman, and S. Henry, "Modeling rough-surface and granular scattering at terahertz frequencies using the finite-difference time-domain method," *IEEE Trans. Geosci. Remote Sens.*, Vol. 48, No. 10, 3709–3719, 2010.

10. Schecklman, S., L. M. Zurk, S. C, Henry, and G. P. Kniffin, "Terahertz material detection from diffuse surface scattering," *J. Appl. Phys.*, Vol. 109, No. 9, 2011.

11. Bandyopadhyay, A., A. Sengupta, R. B. Barat, D. E. Gary, and J. F. Federici, "Grain size dependent scattering studies of common materials using THz time domain techniques," *Proc. SPIE Int. Soc. Opt. Eng.*, Vol. 6120, 2006.

12. Bandyopadhyay, A., A. Sengupta, R. B. Barat, D. E. Gary, J. F. Federici, M. Chen, and D. B. Tanner, "Effects of scattering on THz spectra of granular solids," *Int. J. Infrared Millim. Waves*, Vol. 28, No. 11, 969–978, 2007.

13. Chau, K. J., S. Mujumdar, and A. Y. Elezzabi, "Terahertz propagation in non-homogeneous strongly scattering media," *Proc. SPIE Int. Soc. Opt. Eng.*, Vol. 5727, 177–185, 2005.

14. Pearce, J. and D. M. Mittleman, "Scale model experimentation: Using terahertz pulses to study light scattering," *Phys. Med. Biol.*, Vol. 47, No. 21, 3823–3830, 2002.

15. Pearce, J. and D. M. Mittleman, "Using terahertz pulses to study light scattering," *Physica B-Condensed Matter*, Vol. 338, No. 1–4,

92–96, 2003.

16. Fletcher, J. R., G. P. Swift, D. C. Dai, J. A. Levitt, and J. M. Chamberlain, "Propagation of terahertz radiation through random structures: An alternative theoretical approach and experimental validation," *J. Appl. Phys.*, Vol. 101, No. 1, 2007.

17. Zhang, X.-C., "Terahertz wave imaging: Horizons and hurdles," *Phys. Med. Biol.*, Vol. 47, No. 21, 3667–3677, 2002.

18. Ishimaru, A., *Wave Propagation and Scattering in Random Media*, IEEE Press-Oxford University Press, 1997.

19. Chandrasekhar, S., *Radiative Transfer*, Dover Publications, Inc., 1960.

20. Shin, R. T. and J. A. Kong, "Radiative transfer theory for active remote sensing of a homogeneous layer containing spherical scatterers," *J. Appl. Phys.*, Vol. 52, No. 6, 4221–4230, 1981.

21. Tsang, L. and J. A. Kong, "Radiative transfer theory for scattering by layered media," *J. Appl. Phys.*, Vol. 50, No. 4, 2465–2469, 1979.

22. Fung, A. K. and H. J. Eom, "Application of a combined rough surface and volume scattering theory to sea ice and snow backscatter," *IEEE Trans. Geosci. Remote Sens.*, Vol. GE-20, No. 4, 528–536, 1982.

23. Ma, Q., A. Ishimaru, P. Phu, and Y. Kuga, "Transmission, reflection, and depolarization of an optical wave for a single leaf," *IEEE Trans. Geosci. Remote Sens.*, Vol. 28, No. 5, 865–872, 1990.

24. Tsang, L., C. Chen, A. Chang, J. Guo, and K. Ding, "Dense media radiative transfer theory based on quasicrystalline approximation with applications to passive microwave remote sensing of snow," *Radio Sci.*, Vol. 35, No. 3, 731–749, 2000.

25. Tsang, L., J. Pan, D. Liang, Z. Li, D. Cline, and Y. Tan, "Modeling active microwave remote sensing of snow using dense media radiative transfer (DMRT) theory with multiple-scattering effects," *IEEE Trans. Geosci. Remote Sens.*, Vol. 45, No. 4, 990–1004, 2007.

26. Wen, B., L. Tsang, D. P. Winebrenner, and A. Ishimaru, "Dense medium radiative transfer theory: Comparison with experiment and application to microwave remote sensing and polarimetry," *IEEE Trans. Geosci. Remote Sens.*, Vol. 28, No. 1, 46–59, 1990.

27. Tsang, L. and J. A. Kong, *Scattering of Electromagnetic Waves, Volume 3, Advanced Topics*, John Wiley and Sons, 2001.

28. Nam, K., "Modeling terahertz diffuse scattering from granular media using radiative transfer theory," Master's Thesis, Portland

State University, 2011.

29. Tsang, L. and J. A. Kong, *Scattering of Electromagnetic Waves, Volume 1, Theories and Applications*, John Wiley and Sons, 2000.

30. SmallParts.com, c/o Amazon.com, LLC, P. O. Box 81226, Seattle, WA 98108–1300, United States.

31. Zurk, L. M., L. Tsang, K. H. Ding, and D. P. Winebrenner, "Monte Carlo simulations of the extinction rate of densely packed spheres with clustered and nonclustered geometries," *J. Opt. Soc. Am. A*, Vol. 12, No. 8, 1772–1781, 1995.

32. Zurk, L. M., L. Tsang, and D. P. Winebrenner, "Scattering properties of dense media from Monte Carlo simulations with application to active remote sensing of snow," *Radio Sci.*, Vol. 31, No. 4, 803–819, 1996.

33. Ordal, M. A., R. J. Bell, R. W. Alexander, Jr, L. L. Long, and M. R. Querry, "Optical properties of fourteen metals in the infrared and far infrared: Al, Co, Cu, Au, Fe, Pb, Mo, Ni, Pd, Pt, Ag, Ti, V, and W," *Applied Optics*, Vol. 24, No. 24, 4493–4499, 1985.

34. Ketprom, U., Y. Kuga, S. Jaruwatanadilok, and A. Ishimaru, "Experimental and numerical analysis of polarized light through random distributed spherical particles," *Proc. SPIE Int. Soc. Opt. Eng.*, Vol. 4819, 35–45, 2002.